Inorg. Chem. **2006**, *45*, 8973–8979

$In(OH)_3$ and In_2O_3 Nanorod Bundles and Spheres: Microemulsion-Mediated Hydrothermal Synthesis and Luminescence Properties

Jun Yang, Cuikun Lin, Zhenling Wang, and Jun Lin*

Key Laboratory of Rare Earth Chemistry and Physics, Changchun Institute of Applied Chemistry, Chinese Academy of Sciences, Changchun 130022, People's Republic of China, and Graduate School of the Chinese Academy of Sciences, Beijing 100049, People's Republic of China

Received May 29, 2006

Indium hydroxide, $In(OH)_3$, nano-microstructures with two kinds of morphology, nanorod bundles (around 500 nm in length and 200 nm in diameter) and caddice spherelike agglomerates (around 750–1000 nm in diameter), were successfully prepared by the cetyltrimethylammonium bromide (CTAB)/water/cyclohexane/*n*-pentanol microemulsion-mediated hydrothermal process. Calcination of the $In(OH)_3$ crystals with different morphologies (nanorod bundles and spheres) at 600 °C in air yielded In_2O_3 crystals with the same morphology. X-ray diffraction, scanning electron microscopy, transmission electron microscopy, and photoluminescence (PL) spectra as well as kinetic decays were used to characterize the samples. The pH values of microemulsion play an important role in the morphological control of the as-formed $In(OH)_3$ nano-microstructures from the hydrothermal process. The formation mechanisms for the $In(OH)_3$ nano-microstructures have been proposed on an aggregation mechanism. In_2O_3 nanorod bundles and spheres show a similar blue emission peaking around 416 and 439 nm under the 383-nm UV excitation, which is mainly attributed to the oxygen vacancies in the In_2O_3 nano-microstructures.

1. Introduction

Semiconductor nanostructures have been attracting increasing attention because of their exceptional properties, which differ from those of their bulk counterparts, and their potential applications in optoelectronic devices. Among them, indium oxide (In_2O_3) has been investigated extensively for its semiconducting properties. In_2O_3 is a very important wide-band-gap (direct band gap around 3.6 eV), n-type transparent semiconductor and has been widely used in microelectronic areas including window heaters, solar cells, liquid-crystal displays,[1] and ultrasensitive gas sensors for detection of O_3,[2] CO_2,[3] H_2,[3,4] NO_2,[4] and Cl_2.[5] Inorganic particles often show unique size- and shape-dependent properties. For instance, the gas-sensing ability of In_2O_3 has been shown to increase significantly by decreasing its particle size.[6] It is imaginable that size- and shape-controllable growth of In_2O_3 nanoparticles might pave the way to further elevate its performance. Up to now, various morphologies of In_2O_3 have been synthesized via different methods. For example, In_2O_3 nanobelts through thermal evaporation,[7] In_2O_3 nanowries by using the vapor−liquid−solid technique,[8] In_2O_3 nanoparticles prepared from thermal decomposition,[9] tin-doped In_2O_3 whiskers formed by the electron shower physical vapor deposition process,[10] In_2O_3 nanowire arrays,[11] and nanorods[12] induced by template-assisted growth have been reported. However, there are relatively few reports about the hydrothermal synthesis of In_2O_3 nanostructures.[13,14]

In recent years, soft templates such as reverse micelles or microemulsions have been widely used as an ideal media to prepare inorganic nanoparticles.[15] As the nanosized water

* To whom correspondence should be addressed. E-mail: jlin@ciac.jl.cn.

(1) Hamberg, I.; Granqvist, C. G. *J. Appl. Phys.* **1986**, *60*, 123.
(2) Gagaoudakis, E.; Bender, M.; Douloufakis, E.; Kataarakis, N.; Natsakou, N.; Cimalla, V.; Kiriakids, G. *Sens. Actuator, B* **2001**, *80*, 155.
(3) Chung, W. Y.; Sakai, G.; Shimanoe, K.; Miura, N.; Lee, D. D.; Yamazoe, N. *Sens, Actuator, B* **1998**, *46*, 139.
(4) Liess, M. *Thin Solid Films* **2002**, *410*, 183.
(5) Tamaki, J.; Naruo, C.; Yamanoto, Y.; Matsuoka, M. *Sens. Actuator, B* **2002**, *83*, 190.
(6) Gurlo, A.; Ivanovskaya, M.; Barsan, N.; Schweizer-Berberich, M.; Weimar, U.; Gopel, W.; Dieguez, A. *Sens. Actuators, B* **1997**, *44*, 327.
(7) Pan, Z. W.; Dai, Z. R.; Wang, Z. L. *Science* **2001**, *291*, 1947.
(8) Li, C.; Zhang, D.; Han, S.; Liu, X.; Tang, T.; Zhou, C. *Adv. Mater.* **2003**, *15*, 143.
(9) Seo, W. S.; Jo, H. H.; Lee, K.; Park, J. T. *Adv. Mater.* **2003**, *15*, 795.
(10) Yumoto, H.; Sako, T.; Gotoh, Y.; Nishiyama, K.; Kaneko, T. *J. Cryst. Growth* **1999**, *203*, 136.
(11) Zheng, M. J.; Zhang, L. D.; Li, G. H. *Appl. Phys. Lett.* **2001**, *79*, 839.
(12) Kuo, C. Y.; Lu, S. Y.; Wei, T. Y. *J. Cryst. Growth* **2005**, *285*, 400.

10.1021/ic060934+ CCC: $33.50
Published on Web 10/05/2006

pools, they have been widely used as spatially constrained nanoreactors for controlled synthesis of nanoparticles with a desired narrow size distribution such as Ag nanodisks,[16] CdS nanotriangles,[17] V_2O_5 nanowires/nanorods,[18] $CaCO_3$ nanowires,[19] and $BaSO_4$ filaments cones.[20] At the same time, the combination of microemulsion techniques with a hydrothermal/solvothermal process has also been explored for the preparation of nanocrystals such as ZnS nanocrystallites,[21] CdS nanorods,[22] $SbSO_4$ nanorods,[23] $SrCO_3$ nanostructures,[24] $Ca_{10}(PO_4)_6(OH)_2$ nanofibers,[25] ZnO nanowires,[26] TiO_2 nanocrystallites,[27] SnO_2 nanorods,[28] BaF_2 whiskers,[29] and molecular sieve fibers.[30]

Enlightened by the above reports, we believe that it is reasonable to prepare $In(OH)_3$ or In_2O_3 nanostructures via microemulsion-mediated hydrothermal synthesis. In this paper, we first report the synthesis of $In(OH)_3$ nanomicrostructures with different morphologies (nanorod bundles and spheres) in a cetyltrimethylammonium bromide (CTAB)/water/cyclohexane /*n*-pentanol microemulsion system under hydrothermal conditions by carefully controlling fundamental experimental parameters such as the pH values of the microemulsion. The obtained $In(OH)_3$ nanorod bundles and spheres, both consisting of individual nanoparticles with size ranging from 30 to 55 nm, can be efficiently achieved at a hydrothermal temperature as low as 140 °C. To the best of our knowledge, this is the lowest temperature reported by far for the fabrication of $In(OH)_3$ crystals through the hydrothermal process. Calcination of the $In(OH)_3$ crystals yielded In_2O_3 crystals with the same morphology. Finally, the optical properties of the resulting In_2O_3 nano-microstructures were investigated.

2. Experimental Section

Preparation. All of the chemicals used in our experiment were of analytical-reagent (A.R.) grade, purchased from Beijing Fine Chemical Co., Beijing, China. A quaternary microemulsion system consisting of cetyltrimethylammonium bromide (CTAB)/water/cyclohexane/*n*-pentanol was selected for this study. The microemulsion was prepared by dissolving CTAB (1.0 g) in 30 mL of cyclohexane and 1.5 mL of *n*-pentanol. The mixing solution was stirred for 30 min. Then a certain volume of a 0.5 M $In(NO_3)_3$ aqueous solution was added to the solution. The molar ratio of water to CTAB was set at 5, and the pH value of the microemulsion was changed from 5 to 3 through the addition of drops of concentrated nitric acid. The solution was stirred for another 60 min. Then the transparent feedstock was charged into a 45-mL Teflon-lined stainless steel autoclave and heated at 140 °C for 24 h. After the autoclave was cooled to room temperature naturally, the precursors were separated by centrifugation, washing with ethanol and distilled water several times, and drying in an air atmosphere at 60 °C for 4 h. The final products were retrieved through a heat treatment at 600 °C for 2 h in air. To investigate the growing process for $In(OH)_3$ crystals with different morphologies, the hydrothermal reactions were stopped after designed times of 1.5, 5.5, 16, and 24 h (for nanorod bundles) or 4, 7, 16, and 24 h (for nanorod spheres), respectively. Then the products were isolated and analyzed.

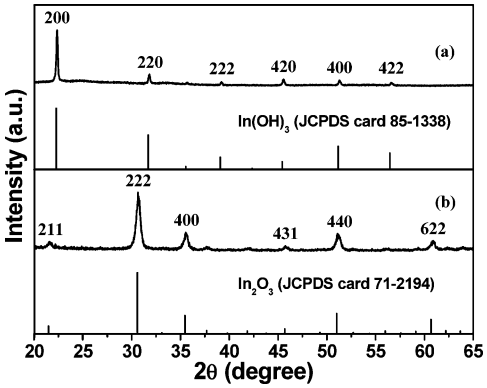

Figure 1. XRD patterns of the as-formed sample (a) and that after annealing at 600 °C (b). The standard data for $In(OH)_3$ (JCPDS No. 85-1338) and In_2O_3 (JCPDS No. 71-2194) are also presented in the figure for comparison.

Characterization. The samples were characterized by powder X-ray diffraction (XRD) performed on a Rigaku-Dmax 2500 diffractometer with Cu Kα radiation (λ = 0.154 05 nm). The morphology of the samples was inspected using a field emission scanning electron microscope (Philips XL 30) equipped with an energy-dispersive spectrometer and a transmission electron microscope (JEOL-2010, 200 kV). Photoluminescence (PL) excitation and emission spectra were recorded with a Hitachi F-4500 spectrophotometer equipped with a 150-W xenon lamp as the excitation source at room temperature. The luminescence decay curves were obtained using a Lecroy Wave Runner 6100 digital oscilloscope (1 GHz) and a 383-nm UV laser (pulse width = 4 ns) as the excitation source.

3. Results and Discussion

3.1. Phase Formation. Figure 1 shows the XRD patterns of the as-formed products through the hydrothermal process (a) and those after a heat treatment at 600 °C (b). The XRD peaks for as-formed samples can be indexed to a cubic lattice [space group: $Im\bar{3}(204)$] of pure indium hydroxide, $In(OH)_3$, as shown in Figure 1a. The calculated lattice constant, a = 0.7977 nm, is in good agreement with that (a = 0.7979 nm) from the standard card (JCPDS No. 85-1338). After anneal-

(13) Tang, Q.; Zhou, W.; Zhang, W.; Ou, S.; Jiang, K.; Yu, W.; Qian, Y. T. *Cryst. Growth Des.* **2005**, *5*, 147.
(14) Yu, D.; Yu, S. H.; Zhang, S.; Zuo, J.; Wang, D.; Qian, Y. T. *Adv. Funct. Mater.* **2003**, *13*, 497.
(15) (a) Schwuger, M.; Stickdom, K.; Schomacker, R. *Chem. Rev.* **1995**, *95*, 849. (b) Gan, L. M.; Liu, B.; Chew, C. H.; Xu, S. J.; Chua, S. J.; Loy, G. L.; Xu, G. Q. *Langmuir* **1997**, *13*, 6427. (c) Feng, P.; Bu, X.; Stucky, G. D.; Pine, D. J. *J. Am. Chem. Soc.* **2000**, *122*, 994.
(16) Maillard, M.; Giorgio, S.; Pileni, M. P. *Adv. Mater.* **2002**, *14*, 1084.
(17) (a) Pinna, N.; Weiss, K.; Kongehl, H. S.; Vogel, W.; Urban, J.; Pileni, M. P. *Langmuir* **2001**, *17*, 7982. (b) Pinna, N.; Weiss, K.; Urban, J.; Pilent, M. P. *Adv. Mater.* **2001**, *13*, 261.
(18) Pinna, N.; Willinger, M.; Weiss, K.; Urban, J.; Schlogl, R. *Nano Lett.* **2003**, *3*, 1131.
(19) Kuang, D. B.; Xu, A. W.; Fang, Y. P.; Ou, H. D.; Liu, H. Q. *J. Cryst. Growth* **2002**, *244*, 379.
(20) (a) Hopwood, J. D.; Stephen, M. *Chem. Mater.* **1997**, *9*, 1819. (b) Li, M.; Stephen, M. *Langmuir* **2000**, *16*, 7088.
(21) Xu, S. J.; Chua, S. J. *Appl. Phys. Lett.* **1998**, *73*, 478.
(22) Zhang, P.; Gao, L. *Langmuir* **2003**, *19*, 208.
(23) Xiang, J. H.; Yu, S. H.; Geng, X.; Liu, B. H.; Xu, Y. *Cryst. Growth Des.* **2005**, *5*, 1157.
(24) Cao, M. H.; Wu, X. L.; He, X. Y. *Langmuir* **2005**, *21*, 6093.
(25) Cao, M. H.; Wang, Y. H.; Guo, C. X. *Langmuir* **2004**, *20*, 4784.
(26) Zhang, J.; Sun, L. D.; Pan, H. Y. *New J. Chem.* **2002**, *26*, 33.
(27) (a) Wu, M. M.; Long, J. B.; Huang, A. H.; Luo, Y. J. *Langmuir* **1999**, *15*, 8822. (b) Andersson, M.; Osterlund, L.; Ljungstrom, S.; Palmqvist, A. *J. Phys. Chem. B* **2002**, *106*, 10674.
(28) Zhang, D. F.; Sun, L. D.; Yin, J. L.; Yan, C. H. *Adv. Mater.* **2003**, *15*, 1022.
(29) Cao, M. H.; Hu, C. W.; Wang, E. B. *J. Am. Chem. Soc.* **2003**, *125*, 11196.
(30) Lin, J. C.; Dipre, J. T.; Yates, M. Z. *Chem. Mater.* **2003**, *15*, 2764.

ing at 600 °C in air, the XRD pattern of the resulting sample exhibits multiple intense peaks, all of which can be perfectly indexed to the cubic phase [space group: $Ia\bar{3}(206)$] of In_2O_3, as shown in Figure 1b. The calculated lattice parameter (a = 1.0125 nm) for In_2O_3, is in good agreement with the known lattice parameter for crystalline In_2O_3 (a = 1.0117 nm; JCPDS No. 71-2194). The crystallite size of the samples can be estimated from the Scherrer equation, $D = 0.941\lambda/\beta \cos\theta$, where D is the average grain size, λ is the X-ray wavelength (0.154 05 nm), and θ and β are the diffraction angle and full-width at half-maximum (fwhm) of an observed peak, respectively.[31] The strongest peaks (200) at 2θ = 22.30° and (222) at 2θ = 30.62° were used to calculate for the average crystallite size (D) of the In(OH)$_3$ and In_2O_3 particles, respectively. The estimated average crystallite sizes are about 60 nm for In(OH)$_3$ particles and 25 nm for In_2O_3 particles.

The synthesis reactions can be simply expressed as

$$In^{3+} + 3H_2O \rightarrow In(OH)_3 + 3H^+ \quad (1)$$

$$2In(OH)_3 \rightarrow In_2O_3 + 3H_2O \quad (2)$$

Under the hydrothermal process, In(OH)$_3$ nano-microstructures are prepared by the hydrolysis reaction of In^{3+} at 140 °C, as described in reaction (1). The dehydration of the In(OH)$_3$ precursors at 600 °C results in the formation of the final product In_2O_3 nano-microstructures, as described in reaction (2).

3.2. Morphology Control. The pH values of the microemulsion have great effects on the morphology of the hydrothermal products. Figure 2a shows the SEM images of the as-formed In(OH)$_3$ samples prepared from the microemulsion system with pH = 5. It can be seen that the In(OH)$_3$ samples are composed of uniform nanorod bundles (around 500 nm in length and 200 nm in diameter) with an aspect ratio of about 2.5:1, and the nanorod bundles consist of individual parallel nanorods with diameters ranging from 30 to 45 nm. Every nanorod is further composed of the smaller nanosized particles with size ranging from 30 to 45 nm, basically in the same size range as those estimated by XRD. The inset in Figure 2a is the magnified image of In(OH)$_3$ nanorod bundles. After calcination at 600 °C, the obtained In_2O_3 samples retain the morphology and size of In(OH)$_3$, as shown in Figure 2b. The chemical composition of the In_2O_3 nanorod bundles was investigated with energy-dispersive spectrometry (EDS; Figure 2c), which indicates an atomic ratio of In:O = 2:2.94. The deviation from In:O = 2:3 may be due to the experimental error of EDS experiments. The EDS result gives further support for the XRD analysis above. To further study the fine structure of the above nanorod bundles, transmission electron microscopy (TEM) was performed. Representative TEM micrographs for the In(OH)$_3$ and In_2O_3 nanorod bundles are shown in parts a−d of Figure 3. As can be seen from Figure 3a, In(OH)$_3$ nanorod bundles with a width of about 210 nm and a length

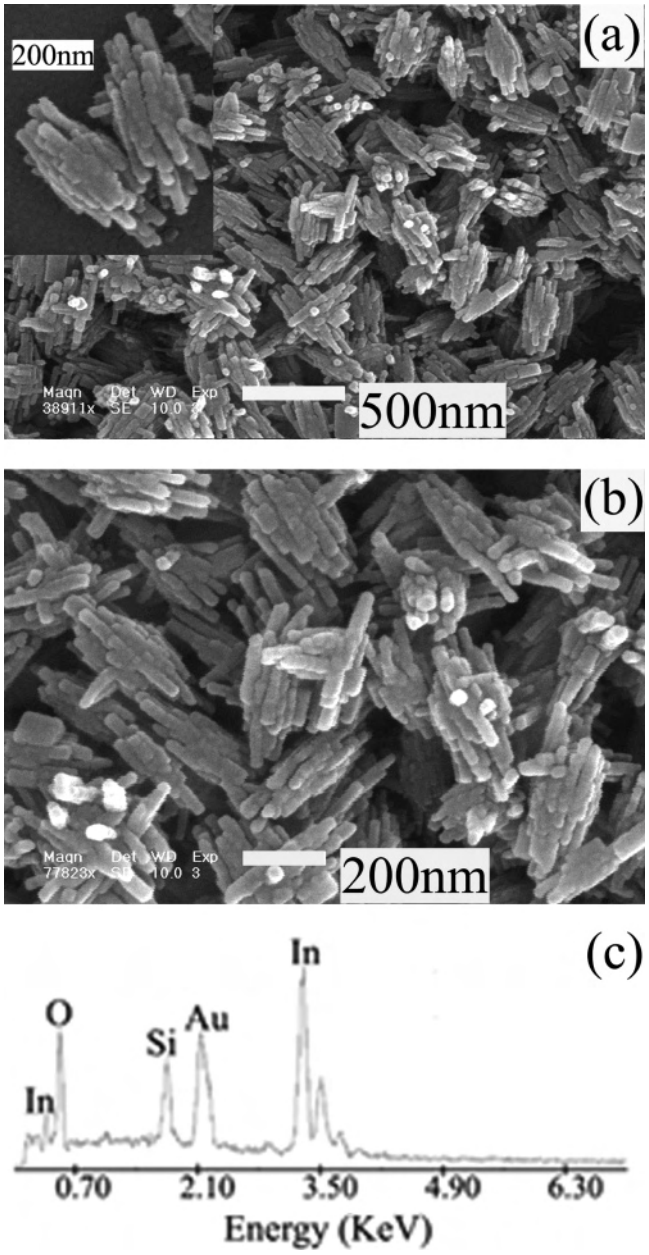

Figure 2. Field emission scanning electron micrsocopy (FE-SEM) images of the as-formed hydrothermal products of In(OH)$_3$ (a) and the corresponding In_2O_3 (b) obtained from the microemulsion with pH = 5. The inset in part a is the magnified image of an individual In(OH)$_3$ nanorod bundle. EDS of the In_2O_3 nanorod bundles (c) found In and O from the sample with an atom ratio of In:O = 2:2.94 (Au from the Au coating and Si from the Si substrate were used for measurement).

of about 500 nm are obtained, which is composed of parallel nanorods with a mean diameter of 40 nm. High-resolution TEM and selected-area electron diffraction (SAED) were performed in the region of nanorod bundles as labeled in Figure 3a, and the micrographs are shown in parts b and c of Figure 3, respectively. The lattice fringes of crystalline In(OH)$_3$ can be seen clearly (Figure 3b); the SAED images, which combine partial ring and dot patterns, indicate that the nanorod is of polycrystalline nature. Figure 3d is the TEM image of the In_2O_3 nanorod bundles, which is in agreement with the SEM results (Figure 2b). The average diameter of the nanorod (the subunit of nanorod bundles) of In_2O_3

(31) Zhang, Y. W.; Jin, S.; Tian, S. J.; Li, G. B.; Jia, T.; Liao, C. S.; Yan, C. H. *Chem. Mater*. **2001**, *13*, 372.

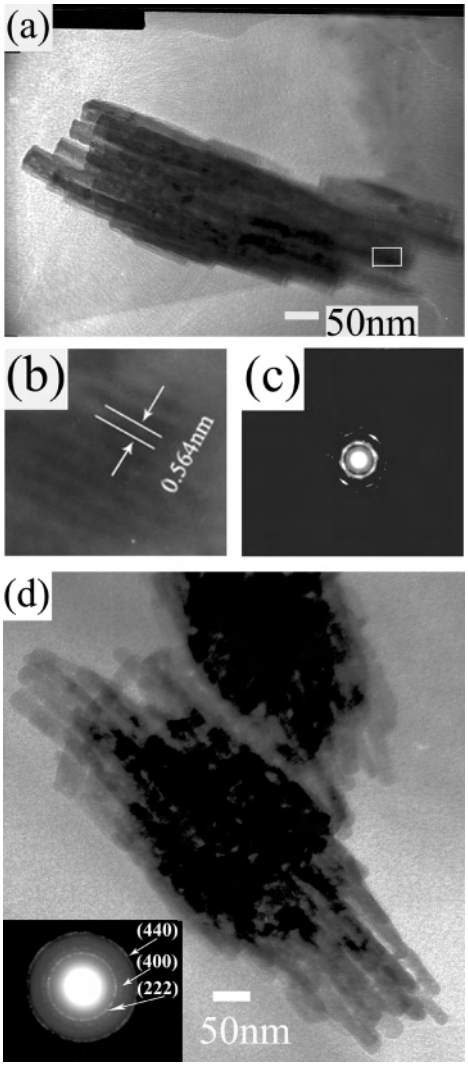

Figure 3. TEM images of the as-formed hydrothermal products of $In(OH)_3$ (a) with its HRTEM (b) and SAED pattern (c) as well as the TEM image of the In_2O_3 nanorod bundles (d) with the SAED pattern (inset).

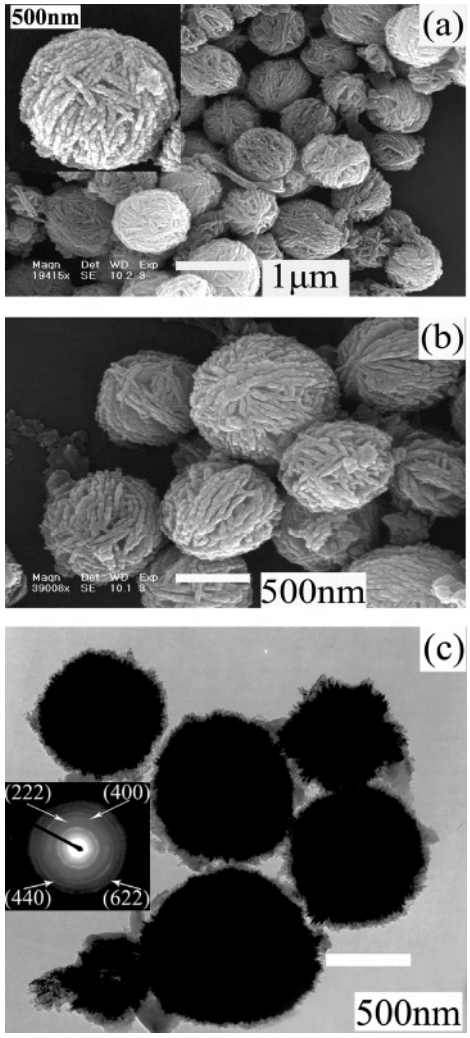

Figure 4. FE-SEM images of the as-formed hydrothermal products of $In(OH)_3$ (a) and the corresponding In_2O_3 (b) with its TEM image (the SAED pattern in the inset) of the In_2O_3 spheres (c) obtained from the microemulsion with pH = 3. The inset in part a is the magnified image showing an individual $In(OH)_3$ sphere.

reduces to 20−30 nm compared with that of $In(OH)_3$ in Figure 3a (mean diameter of 40 nm), indicating that the decomposition of $In(OH)_3$ resulted in a reduction of the particle size in In_2O_3. There are some dark parts on the TEM image because those parts may be too thick for the electrons to penetrate. The SAED of In_2O_3 nanorod bundles is given in the inset of Figure 3d, whose strong diffraction rings can be indexed as (222), (400), and (440) planes of cubic In_2O_3.

When the pH value of the microemulsion was decreased to 3, the hydrothermal product of $In(OH)_3$ consisted of caddice spherelike agglomerates (instead of the nanorod bundles for pH = 5), as shown in the SEM image of Figure 4a. The diameters of the spherical agglomerates of $In(OH)_3$ are in the range of 0.75−1 μm. Clearly, the individual $In(OH)_3$ sphere seems to be also composed of crooked nanorods with diameters ranging from 30 to 55 nm, and each nanorod contains smaller nanosized particles with sizes ranging from 30 to 55 nm. The initial shape and size of the products are basically kept in the phase transformation from $In(OH)_3$ to In_2O_3 after calcination at 600 °C (Figure 4b). Figure 4c is the TEM image of the In_2O_3 spheres. In agreement with the SEM results (Figure 4b), from Figure 4c we can distinctly see that there are many rods grown on the surface of the black spheres, which sustains the fact that the In_2O_3 spheres are composed of nanorods. These spheres are well crystallized, which can be corroborated by the SAED pattern of the sample (inset of Figure 4c). The SAED of the spheres is consistent with cubic In_2O_3 with strong ring patterns due to (222), (400), (440), and (622) planes.

3.3. Formation Mechanism for the $In(OH)_3$ Nanomicrostructures. In principle, crystal growth and crystal morphology are governed by the degree of supersaturation, the diffusion of the reaction, the species to the surface of the crystals, the surface and interfacial energies, and the structure of the crystals; that is, extrinsic and intrinsic factors, the crystal structure, and the growth surroundings are accounted for in the final morphology.[13]

From the above experimental results, it can be seen that the pH value of the microemulsion has a significant effect on the morphologies and sizes of the final products. Furthermore, it was found that the sizes of the crystals obtained by this microemulsion-mediated hydrothermal

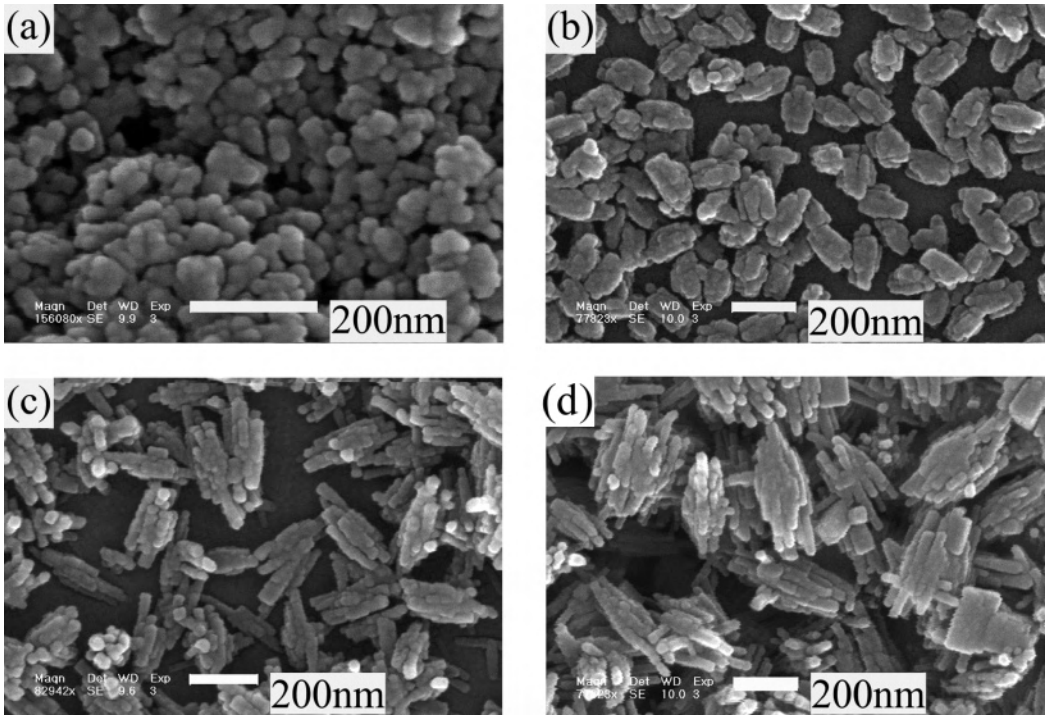

Figure 5. FE-SEM images of In(OH)$_3$ samples at different hydrothermal growing stages (pH = 5): (a) 1.5 h; (b) 5.5 h; (c) 16 h; (d) 24 h.

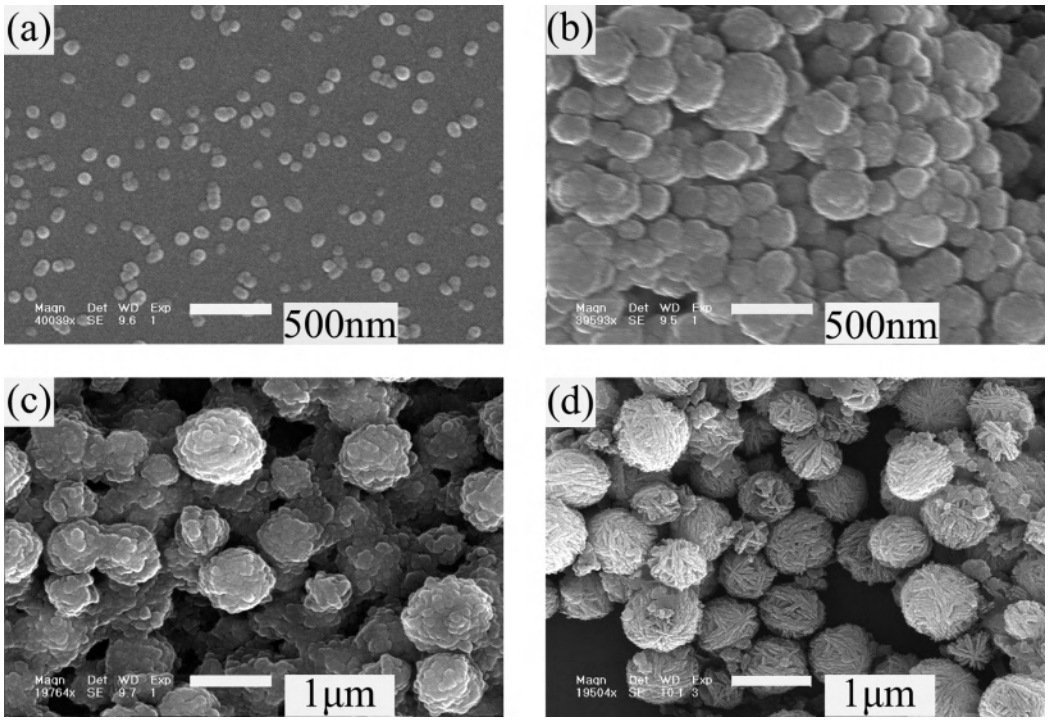

Figure 6. FE-SEM images of In(OH)$_3$ samples at different hydrothermal growing stages (pH = 3): (a) 4 h; (b) 7 h; (c) 16 h; (d) 24 h.

process are much larger than the typical dimensions for individual microemulsion droplets (around 5−100 nm) under appropriate reaction conditions.[24] Thus, it can be inferred that both the pH value of the microemulsion and aggregation and coalescence of individual nanoparticles (formed from the microemulsion droplets) are responsible for the formation of products with different morphologies mentioned in the last section.

The growing process of In(OH)$_3$ nanorod bundles and spherical agglomerates through the hydrothermal process was investigated by observing the images of In(OH)$_3$ crystals at different stages (i.e., different hydrothermal treatment times from 1.5 to 24 h), as shown in Figure 5 (pH = 5) and Figure 6 (pH = 3). The primary particles of In(OH)$_3$ nanoparticles of about 40 nm in diameter can be seen clearly in Figure 5a for t = 1.5 h. Then the crystal nuclei start growing as rodlike crystals (Figure 5b; t = 5.5 h). Afterward, the rodlike crystals became larger and clearer (Figure 5c; t = 16 h). Finally, the uniform nanorod bundles formed (Figure 5d; t = 24 h). In Figure 6, the primary particles of In(OH)$_3$ (about 55 nm in

diameter) just appear after a hydrothermal treatment of 4 h (Figure 6a). Then the crystal nuclei aggregate to bigger spherical agglomerates (Figure 6b for $t = 7$ h and Figure 6c for $t = 16$ h). Finally, the nanoparticles on the surface of the sphere rotate and twist, so the caddice spherelike agglomerates formed (Figure 6d; $t = 24$ h).

On the basis of the series of experimental data, we believe that, in this case, the formation of $In(OH)_3$ rod bundles and spheres belongs to an aggregation growing process. This mechanism indicates that uniform particle formation usually proceeds in several stages. In the initial induction stage, solutes are formed to yield a supersaturated solution, leading to nucleation. The nuclei then grow by a diffusive mechanism to form crystalline subunits, which, in turn, aggregate to form the large polycrystalline assemblages. The impetus for aggregation of nanoparticles is to eliminate the surface energy, which is similar to the SnO_2 nanorods in a solvothermal colloid system.[28] First uniform $In(OH)_3$ nanoparticles formed by a hydrolysis reaction of In^{3+} under hydrothermal conditions in the water pools of the microemulsion system. Then the resulting $In(OH)_3$ nanoparticles were rearranged to find a place to minimize the surface energy. The initial pH conditions of the microemulsion led to different morphologies from nanorod bundles to spheres. This can be ascribed to the fact that under a higher pH value (pH = 5) the nucleating process occurred faster and more crystal nuclei formed. These crystal nuclei in the particle aggregates grew along the same direction (oriented attachment) simultaneously to form nanorod bundles. However, the lower pH value (pH = 3) altered the electric charge distributing on the surface of the nanoparticles, CTAB adsorbed on the different crystal faces,[32] and the surface energy of the nanoparticles compared with samples under higher pH values. Those crystal nuclei in the particle aggregates grew in different directions (random aggregation), rotated, and twisted simultaneously to form spheres (composed of crooked nanorods). Finally, after recrystallization, $In(OH)_3$ nanorod bundles and spheres formed. The whole process is illustrated in Scheme 1.

Scheme 1. Schematic Illustration Showing the Formation Mechanism of $In(OH)_3$ Nanorod Bundles and Spheres

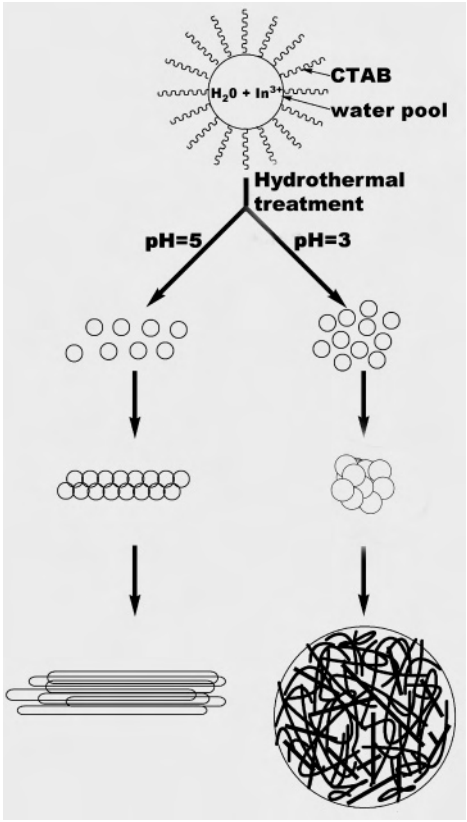

$In(OH)_3$ was converted to In_2O_3 during the subsequent calcination as a gradual elimination of water. Nevertheless, the conversion did not lead to a change in the morphology. Such a transformation was common for $In(OH)_3$ compound decomposition.[13,14] The morphologies were maintained perhaps because of the higher activation energies needed for the collapse of these structures.

3.4. Luminescence Properties. The PL properties of the as-formed $In(OH)_3$ and postannealing-produced In_2O_3 samples were investigated here. It is shown that the as-formed $In(OH)_3$ samples (nanorod bundles and spheres) do not exhibit any luminescence under UV light excitation. However, both the In_2O_3 nanorod bundles and spheres show a strong PL emission in the blue spectral region under UV light irradiation, and their PL properties are similar. The room-temperature PL excitation and emission spectra for In_2O_3 nanorod bundles (or spheres) are shown in parts a and b of Figure 7, respectively. The excitation spectrum consists of a broad band from 300 to 425 nm with a maximum at 383 nm due to the band-gap excitation of an In_2O_3 semiconductor.[14] Upon excitation into the band gap of In_2O_3 at 383 nm, the obtained PL spectrum exhibits two well-resolved emission peaks located at 416 and 439 nm, respectively. Parts c and d of Figure 7 show the luminescence decay curves of the In_2O_3 nanorod bundles monitored at emissions of 439 and 416 nm, respectively. These decay curves can be well fitted by a single-exponential function as $I(t) = I_0 \exp(-t/\tau)$, where I_0 is the initial emission intensity at $t = 0$ and τ is the $1/e$ lifetime of the emission center. The lifetimes are determined to be 7.46 ($\pm$0.02) ns for the 439-nm emission and 7.83 ($\pm$0.04) ns for the 416-nm emission. It is known that the perfect crystals of bulk In_2O_3 cannot emit light at room temperature.[33] The emission from our In_2O_3 nanorod bundles and spheres is probably because they contain the same subunits, namely, In_2O_3 nanoparticles. In previous investigations, PL spectra peaking at 480 and 520 nm from In_2O_3 nanoparticles,[34] 450 nm from In_2O_3 nanocubes,[13] and 378, 398, and 420 nm from In_2O_3 nanofibers[14] have been reported. The PL spectra of our In_2O_3 nanorod bundles (or spheres) are basically in the same spectral region as those in the above reports. Generally, the PL from oxide semiconductors is mainly attributed to the oxygen vacancies. The short lifetimes (7.46 ns for the 439-nm emission and 7.83 ns for the 416-nm emission) of In_2O_3 nanorod bundles (or spheres) are

(32) Lee, S. M.; Cho, S. N.; Cheon, J. *Adv. Mater.* **2003**, *15*, 441.

(33) Ohhata, Y.; Shinoki, F.; Yoshida, S. *Thin Solid Films* **1979**, *59*, 255.
(34) Zhou, H. J.; Cai, W. P.; Zhang, L. D. *Appl. Phys. Lett.* **1999**, *75*, 495.

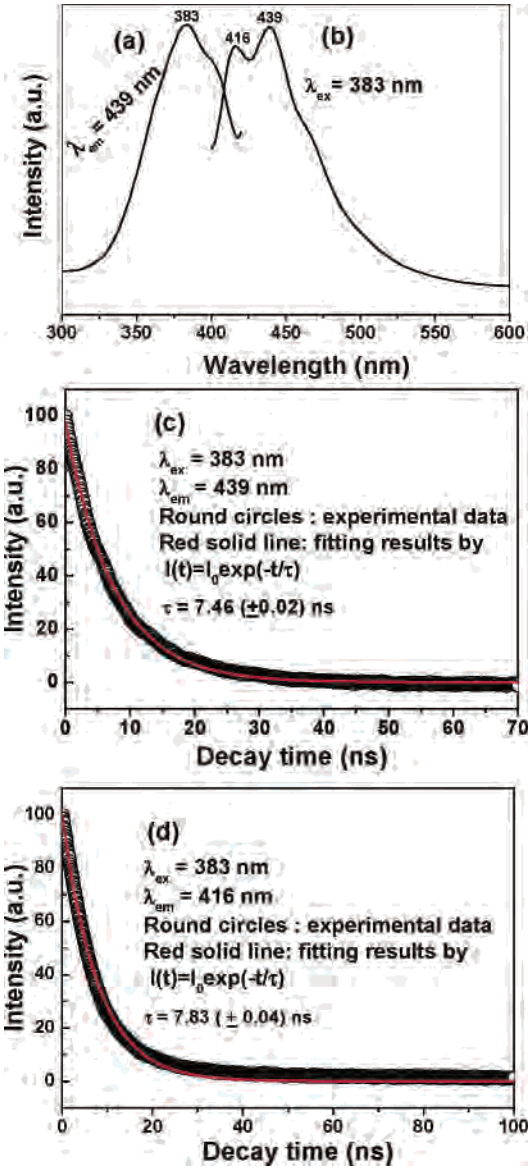

Figure 7. PL excitation (a) and emission (b) spectra of In_2O_3 nanorod bundles as well as the luminescence decay curves for the emissions of 439 nm (c) and 416 nm (d).

typical values for the luminescence caused by defects.[35,36] The oxygen vacancies would induce the formation of new energy levels in the band gap. The blue emission from In_2O_3 nanorod bundles (or spheres) thus results from the radioactive recombination of an electron occupying oxygen vacancies with a photoexcited hole, which is analogous to the PL mechanism of ZnO and SnO_2 semiconductors.[13,37] The blue emission process in In_2O_3 samples can be illustrated in

(35) Fujimaki, M.; Ohki, Y.; Nishikawa, H. *J. Appl. Phys.* **1997**, *81*, 1042.
(36) Pifferi, A.; Taroni, P.; Torricelli, A.; Valentini, G.; Mutti, P.; Ghislotti, G.; Zanghieri, L. *Appl. Phys. Lett.* **1997**, *70*, 348.
(37) Liang, C. H.; Meng, G. W.; Lei, Y. *Adv. Mater.* **2001**, *13*, 1330.

Scheme 2. Simple Schematic Model Illustrating the Excitation and Emission Process for In_2O_3

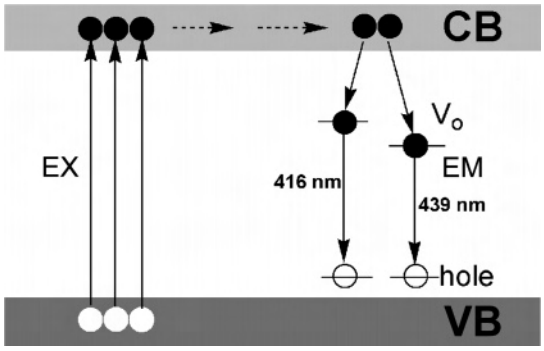

Scheme 2. Under the excitation of 383-nm irradiation, the electrons (●) are excited from the valence band (VB) to the conduction band (CB). The electrons (●) move freely in the CB and finally relax to the oxygen vacancies. The recombination of an electron occupying oxygen vacancies with a photoexcited hole yields the blue emission with maximum wavelengths at 416 and 439 nm. The different emission peaks are related to the different energy levels produced by oxygen vacancies.[14] In this study, the In_2O_3 nanorod bundles and spheres were fabricated from $In(OH)_3$ precursors after annealing at 600 °C, and oxygen vacancies might be generated in the annealing process. In addition, In_2O_3 with peculiar morphologies should also favor the existence of a large amount of oxygen vacancies.

4. Conclusions

In summary, $In(OH)_3$ and In_2O_3 nano-microstructures with nonarod bundles and spheres have been successfully achieved by the microemulsion-mediated hydrothermal method and a subsequent heat treatment process, respectively. The shape and size of $In(OH)_3$ and In_2O_3 can be modulated by the pH value of the microemulsion. The combination of hydrothermal processes and subsequent heat treatment is an effective method for preparing $In(OH)_3$ and In_2O_3 crystals with different morphologies, such as nanorod bundles and spheres. The formation mechanisms for the $In(OH)_3$ nano-microstructures are based on an aggregation process of primary nanoparticles. The as-formed $In(OH)_3$ samples do not exhibit any luminescence, while the In_2O_3 nanorod bundles and spheres show a strong blue emission due to the oxygen vacancies.

Acknowledgment. This project is financially supported by the foundation of "Bairen Jihua" of the Chinese Academy of Sciences, the MOST of China (Grant 2003CB314707), and the National Natural Science Foundation of China (Grants 50225205, 50572103, 20431030, and 00310530).

IC060934+